Inorganic Chemistry

pubs.acs.org/IC Article

Structural, Vibrational, and Electronic Properties of 1D-$TlInTe_2$ under High Pressure: A Combined Experimental and Theoretical Study

Sorb Yesudhas,* N. Yedukondalu,* Manoj K. Jana, Jianbo Zhang, Jie Huang, Bijuan Chen, Hongshang Deng, Raimundas Sereika, Hong Xiao, Stanislav Sinogeikin, Curtis Kenney-Benson, Kanishka Biswas, John B. Parise, Yang Ding,* and Ho-kwang Mao

Cite This: *Inorg. Chem.* 2021, 60, 9320−9331 Read Online

ACCESS | Metrics & More | Article Recommendations | Supporting Information

ABSTRACT: Analogous to 2D layered transition-metal dichalcogenides, the TlSe family of quasi-one dimensional chain materials with the Zintl-type structure exhibits novel phenomena under high pressure. In the present work, we have systematically investigated the high-pressure behavior of $TlInTe_2$ using Raman spectroscopy, synchrotron X-ray diffraction (XRD), and transport measurements, in combination with first principles crystal structure prediction (CSP) based on evolutionary approach. We found that $TlInTe_2$ undergoes a pressure-induced semiconductor-to-semimetal transition at 4 GPa, followed by a superconducting transition at 5.7 GPa (with T_c = 3.8 K). An unusual giant phonon mode (A_g) softening appears at ∼10−12 GPa as a result of the interaction of optical phonons with the conduction electrons. The high-pressure XRD and Raman spectroscopy studies reveal that there is no structural phase transitions observed up to the maximum pressure achieved (33.5 GPa), which is in agreement with our CSP calculations. In addition, our calculations predict two high-pressure phases above 35 GPa following the phase transition sequence as *I*4/*mcm* (B37) → *Pbcm* → $Pm\bar{3}m$ (B2). Electronic structure calculations suggest Lifshitz (L1 & L2-type) transitions near the superconducting transition pressure. Our findings on $TlInTe_2$ open up a new avenue to study unexplored high-pressure novel phenomena in TlSe family induced by Lifshitz transition (electronic driven), giant phonon softening, and electron−phonon coupling.

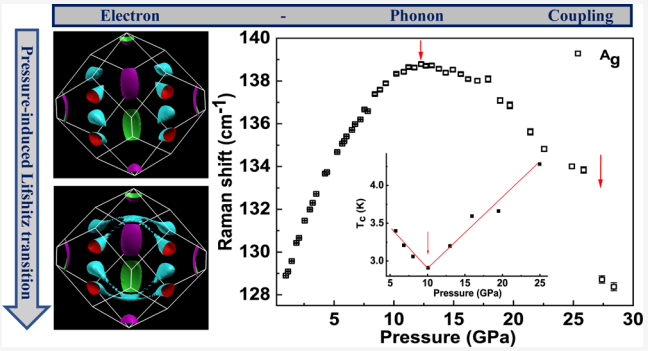

INTRODUCTION

Soon after the discovery of non-trivial topological quantum states in chalcogen-based semiconductors with narrow band gaps and strong spin−orbit coupling (SOC), the two-dimensional (2D) layered semiconductors opened up a new avenue to scrutinize novel pressure-induced phenomena, such as quantum phase transitions, topological superconductors, charge density waves, structural phase transitions, Lifshitz transitions, and so forth.[1−4] In contrast to layered 2D materials, one-dimensional (1D) chain materials from the TlSe family such as $TlInTe_2$, $TlInSe_2$, $TlGaTe_2$, and so forth are relatively under-explored from the perspective of high pressure research,[5,6] although they exhibit astonishing properties at ambient pressure.[7−10] For instance, $TlInSe_2$ exhibits exceptionally high thermoelectric properties, which is correlated to the formation of an incommensurate superlattice.[11] $TlInTe_2$ exhibits a high figure of merit (1.78 for p-doped and 1.84 for n-doped at 300 K) with an intrinsic ultra-low lattice thermal conductivity (<0.5 W/mK in the temperature range 300−673 K) owing to the spatial fluctuation of the Tl^{1+} cation inside the polyhedral framework of a sublattice formed by Tl^{1+} and Te^{2-} ions.[7,8,12−14]

The Zintl-type 1D-chain material, $TlInTe_2$, crystallizes in the body centred tetragonal structure having space group, *I*4/*mcm* (B37) with *Z* = 4, which is iso-structural to the TlSe-family of compounds.[15,16] The unit cell of $TlInTe_2$ has two sublattices, namely, $In^{3+}Te_4^{2-}$ tetrahedral and $Tl^{1+}Te_8^{2-}$ polyhedral (with eight vertices) sublattices. In the $In^{3+}Te_4^{2-}$ sublattice, four Te^{2-} anions are tetrahedrally bonded to an In^{3+} cation, with the corner sharing of Te atoms along the *c*-axis forming an anionic chain. Similarly, the Tl^{1+} cation is loosely bonded to eight Te^{2-} ions in the $Tl^{1+}Te_8^{2-}$ sublattice, forming a cationic chain , where the Tl^{1+} ions spatially fluctuate inside the square

Received: December 27, 2020
Published: June 21, 2021

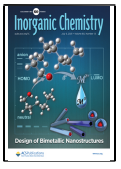

https://doi.org/10.1021/acs.inorgchem.0c03795
Inorg. Chem. 2021, 60, 9320−9331

anti-prismatic (Thomson cube) cage.[12] The Te^{2-} anions in the anionic chains are interconnected via covalent bonding (intrachain bonding), whereas the anionic and cationic chains are connected to each other by weak ionic bonding (interchain bonding). The 1D character of $TlInTe_2$ is due to the formation of 1D chains in its crystal structure, and these chains make $TlInTe_2$ structurally identical to 1D Zintl-type compounds such as Ca_3AlSb_3, $Ca_5Al_2Sb_6$, and so forth.[17,18] The Hall effect studies reported on the isostructural compound, $TlInSe_2$, display different Hall mobility values both along and perpendicular to the chain.[19,20] Thus, the presence of two distinct bonding schemes, such as intrachain and interchain bonding in $TlInTe_2$ combined with its narrow band gap and strong SOC, provide a platform to explore a variety of pressure-induced phenomena including semiconductor to semimetal transition, structural phase transitions, superconductivity, Lifshitz transition, and an incommensurate phase formation (due to the spatial fluctuation of Tl^{1+} cation inside the Thomson cube). The anisotropic bonding scheme in $TlInTe_2$ is anticipated to allow different compression rates along *a* and *c* directions, which may lead to bonding changes, gradual symmetry lowering structural transitions, anisotropic bond length changes, and so forth.[21,22] As a result, the vibrational and transport properties of this compound show anisotropic properties. Interestingly, InTe is iso-structural to $TlInTe_2$, which exhibits superconductivity.[23] Due to an analogous structural relationship between InTe and $TlInTe_2$, we anticipate that $TlInTe_2$ would also exhibit superconductivity under moderate pressure. Strikingly, the monolayer of TlSe (S.G: *I*4/*mcm*) is predicted to be a topological insulator under uniaxial compression[24] while InTe shows a band inversion under hydrostatic pressure.[25] The electronic structure and Fermi surface topology changes under high pressure can provide insights into band inversion and/or electronic topological transitions (including Lifshitz transition).[26−31] Preliminary high-pressure Raman studies on $TlInTe_2$ up to ∼17 GPa suggest phase transition at 7 GPa and signatures of another phase transition at higher pressure.[32] The existence of a high-pressure phase at 7 GPa is still unexplored due to the lack of high-pressure X-ray diffraction (XRD) studies. Similarly, room temperature resistivity measurements carried out along and perpendicular to the *c*- axis of $TlInTe_2$ single crystals showed continuous metallization up to 7 GPa upon cooling to liquid nitrogen temperature.[33] Since there is no systematic high-pressure transport measurements on $TlInTe_2$, in this work, we have investigated high-pressure structural, electronic, vibrational, and superconducting behavior of $TlInTe_2$ using high-pressure Raman spectroscopy, synchrotron XRD, and transport measurements combined with first-principles CSP calculations.

EXPERIMENTAL DETAILS

A detailed synthesis procedure of $TlInTe_2$ powder sample is discussed elsewhere.[12] A symmetric-type diamond anvil cell (DAC) with a culet size of 300 μm was used for both high-pressure synchrotron XRD (HPXRD) and Raman measurements. A stainless-steel gasket was preindented to a thickness of 40 μm and a hole was drilled at its center to a diameter of 150 μm using a laser drilling machine at High-Pressure Collaborative Access Team (HPCAT). A thin pellet size sample about 40 μm was loaded into the sample chamber. HPXRD studies were carried out at 16-BM-D beamline at HPCAT, Advanced Photon Source. The quasi hydrostatic condition was achieved by Ne gas pressure transmitting medium (PTM).[34] The spot size of the X-ray beam used was ∼5 μm, and the X-ray beam diffracted from the sample was detected by an imaging plate detector. The 2D XRD image was converted to a 1D pattern by using Fit2D software,[35] and the XRD data were fitted by using Fullprof Suite software.[36] The pressure was determined by the ruby fluorescence method.[37] Raman measurements were carried out on a Renishaw inVia Raman spectrometer, and the sample was excited by a green laser (λ = 532 nm). The Ne gas was used as PTM for Raman measurements. The Raman data were collected using a CCD detector.

The transport measurements up to 3.9 GPa for the temperatures down to 12 K were carried out with a Janis ST-500 continuous flow cryostat and they were carried out using the Quantum Design physical property measurement system (PPMS) for pressures at 5.7 GPa and above. High pressure was achieved by a Cu−Be DAC, and resistance was measured by four probe method. Boron nitride powder was used to form an insulating gasket for the sample, and 5 μm thick Pt wires were used as electrical leads. No PTM was used for the transport measurements.

COMPUTATIONAL DETAILS

First-principles CSP calculations were carried out using Universal Structure Predictor: Evolutionary Xtallography (USPEX) code based on evolutionary approach.[38−40] We performed an extensive crystal structure search with fixed composition ($TlInTe_2$) at distinct pressures such as ∼ 0, 10, 30, and 50 GPa with 2, 4, and 8 formula units per primitive cell. The first generation with 150 structures is randomly generated, and the succeeding 44 generations with a population size of 50 were obtained by applying heredity (50%), random (20%), soft mutation (20%), and lattice mutation (10%) operators until the best structure remains invariant up to 20 generations. The first-principles calculations were performed within the framework of density functional theory. To obtain the global minimum energy structures, the structural optimization was performed with projector-augmented plane-wave (PAW) potentials,[41] within the generalized gradient approximation of Perdew−Burke−Ernzerhof (PBE) parametrization[42] as implemented in the Vienna Ab initio Simulation Package (VASP).[43] The PAW potentials with $5s^25p^65d^{10}6s^26p^1$, $4s^24p^64d^{10}5s^25p^1$, and $4s^24p^64d^{10}5s^25p^4$ electrons are treated as valence states for Tl, In, and Te respectively. A kinetic energy cutoff of 530 eV was used for the plane wave basis set expansion, and also, $2\pi \times 0.024$ $Å^{-1}$ *k*-spacing was chosen to sample the Brillouin zone.

Electronic structure and Fermi surface topology at high pressure were calculated using the Tran−Blaha-modified Becke Johnson (TB-mBJ) potential[44] as implemented in the WIEN2k package.[45] To achieve energy eigen value convergence, wave functions in the interstitial region were expanded in plane waves with cutoff, K_{max} = 7/RMT, where RMT is the smallest atomic sphere radius and K_{max} denotes the magnitude of largest *k*-vector in plane wave expansion, while the charge density was Fourier expanded up to G_{max} = 14. The muffin-tin radii were assumed to be 2.6 Bohr for Tl and 2.5 Bohr for In and Te atoms.

RESULTS AND DISCUSSION

High-Pressure Raman Spectroscopy. Eight atoms in the primitive cell of $TlInTe_2$ results in 24 (3*N*; where *N* is number of atoms per primitive cell) phonon modes at the Γ-point of the Brillouin zone and the factor group analysis yields

$$\Gamma_{vib} = A_{1g} \oplus 2A_{2g} \oplus B_{1g} \oplus 2B_{2g} \oplus 3E_g \oplus B_{1u} \oplus 3A_{2u} \oplus 4E_u$$

https://doi.org/10.1021/acs.inorgchem.0c03795
Inorg. Chem. 2021, 60, 9320−9331

where the subscripts "g" and "u" denote gerade and ungerade modes, respectively. Out of 24 vibrational modes (3 acoustic and $3N - 3 = 21$ optical), seven are Raman-active and five are IR-active. Since our Raman spectrometer can detect only frequencies above 100 cm^{-1}, we have observed only two Raman active modes, namely, A_g = 127.1 (127)[46] cm^{-1} and E_g = 138.6 (138)[46] cm^{-1} of $TlInTe_2$ at ambient pressure, where the A_g mode represents the opposite and perpendicular motion of adjacent Te^{2-} anions in the *XY* plane and the E_g mode represents the opposite motion of adjacent Te^{2-} ions but all anions in the same plane along with opposite motion of In^{3+} cations, as illustrated in Figure 1.[32,46] The observed Raman

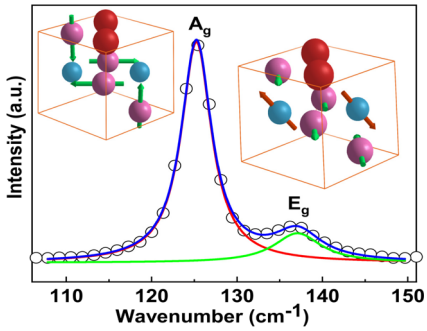

Figure 1. Raman spectrum of $TlInTe_2$ at ambient pressure. The A_g mode represents the opposite and perpendicular motion of adjacent Te^{2-} anions in the *XY* plane and along *z*-axis, whereas the E_g mode indicates the opposite motion of adjacent Te^{2-} ions but all anions in the same plane and opposite motion of In^{3+} cations, respectively. Red, blue, and pink balls represent Tl, In, and Te atoms, respectively. Arrows refer to the displacement direction.

modes in this work are in excellent agreement with the previous Raman measurements[32] as well as with the recent theoretical calculations (A_g = 128.2 and E_g = 138.8 cm^{-1}).[47] Raman spectra of $TlInTe_2$ at different pressures are shown in Figures 2a and S1, and the pressure dependence of Raman modes, A_g and E_g, are plotted in Figure 2b, c. It is evident from Figures 2a and S1 that the intensity of these Raman modes decreases with pressure. The intensity ratio of E_g and A_g modes exhibits a significant change at 4 GPa (Figure 2d). In order to further comprehend the high-pressure behavior of Raman modes, pressure coefficients and mode Grüneisen parameters are calculated by fitting the pressure-frequency data of phonon modes up to 8 GPa to a quadratic equation. The calculated pressure coefficients of A_g and E_g modes are as presented in Table S1 and are closely comparable to the previously reported values.[32] The relative stiffness of the A_g mode, with a pressure coefficient of 1.91 cm^{-1}/GPa compared to that of E_g mode, 3.98 cm^{-1}/GPa, suggests a disparity in the bonding behavior of $TlInTe_2$ [see Table S1].

The bonding behavior and various forces acting on a crystal can be inferred from mode Grüneisen parameters (γ), which are calculated from the above quadratic fit by using the following relationship

$$\gamma(\omega) = \left(\frac{B_0}{\omega_0}\right)\frac{d\omega}{dp}\bigg|_{p=0} \quad (1)$$

where ω_0 is the frequency and B_0 is the bulk modulus at ambient pressure. The calculated B_0 of $TlInTe_2$ is 19.4 GPa (B_0' = 7.3). The calculated γ values of A_g (γ = 0.29) and E_g (γ = 0.56) modes are much smaller compared to the reported values; A_g (γ = 0.81) and E_g (γ = 1.6)[32] (see Table S1), which is due to a large bulk modulus value (B_0 = 58.3 GPa; ∼ 3 times larger than the one obtained in this work) used for calculating the γ values.[32] It is interesting to note that the pressure dependence of the full width at half-maximum (FWHM) of the A_g mode is constant up to 6 GPa, while above this pressure, the phonon line width exhibits a dramatic increase [Figure 2d]. Similarly, the intensity ratio of E_g and A_g modes exhibits a minimum around 6 GPa [see the inset of Figure 2d]. The phonon life time change [FWHM (cm^{-1})] of the A_g mode and a minimum in the intensity ratio of E_g and A_g modes versus pressure hint at another transition at 6 GPa [Figure 2d]. Upon further compression, we observe major changes in the frequency of the A_g phonon mode, as shown in Figure 2b. For instance, an abnormal frequency reversal (softening) of the A_g mode and a subtle softening of the E_g mode are also observed around 10−12 GPa. The A_g mode exhibits frequency discontinuity at 25 GPa. Since Raman spectra (Figure 2) do not provide any explicit evidence of either appearance or disappearance of phonon modes up to the maximum pressure achieved (29 GPa), the origin of these transitions might be unrelated to structural phase transitions. A more detailed investigation of the above transitions are discussed in the subsequent sections with reference to HPXRD, transport measurements, and first-principles CSP calculations.

HPXRD, Structure Prediction, and Stability. To obtain further insights on the nature of transitions observed in high-pressure Raman measurements, HPXRD studies were carried out on $TlInTe_2$. The HPXRD pattern of $TlInTe_2$ for typical pressures (1.1−33.5 GPa) is shown in Figure 3a. The lattice parameters are extracted from the XRD pattern by Le Bail method.[36] Our attempts to perform Rietveld refinement were unsuccessful as some of the calculated peak intensities notably (200) and (211) peaks at 5.73 and 7.23°, respectively, could not fit well with the experimental pattern [Figures S2 and S3]. Although the refinement of anisotropic displacement parameters of Tl and In atoms has slightly improved the fit, still there is a huge intensity mismatch between the experimental and calculated XRD pattern, as shown in Figure S3. A plausible reason for the intensity discrepancy could be due to a large spatial fluctuation of the Tl^{1+} cation inside the Tl^{1+}−Te^{2-} Thomson cube resulting in fluctuating electron density at the Tl Wyckoff site, which alters the structure factor of the Tl atom.[7,48] As a result, the intensity and width of the calculated XRD pattern do not fit with certain peaks because the effective electron density of X-rays seen by the Tl^{1+} cation would be different from its actual value. This argument is further validated by the recent X-ray fluorescence holography (XFH) studies on $TlInTe_2$. The XFH studies reveal that three-dimensional (3D) atomic images around the Tl atoms are weakly visible at the Tl site, whereas the In atoms are completely visible at the In site despite the fact that the X-ray scattering of Tl (Z = 81) is much higher than that of Indium (Z = 49).[49,50] Our HPXRD pattern does not provide any evidence of structural phase transition up to the maximum pressure (33.5 GPa) achieved. Hence, we rule out the possibility of structural phase transition at 7 GPa proposed by Ves using high-pressure Raman spectroscopic measurements.[32]

We have calculated pressure-dependent lattice parameters and equation-of-state (EOS) of $TlInTe_2$ from the HPXRD data. They are plotted together with the theoretical data in

https://doi.org/10.1021/acs.inorgchem.0c03795
Inorg. Chem. 2021, 60, 9320−9331

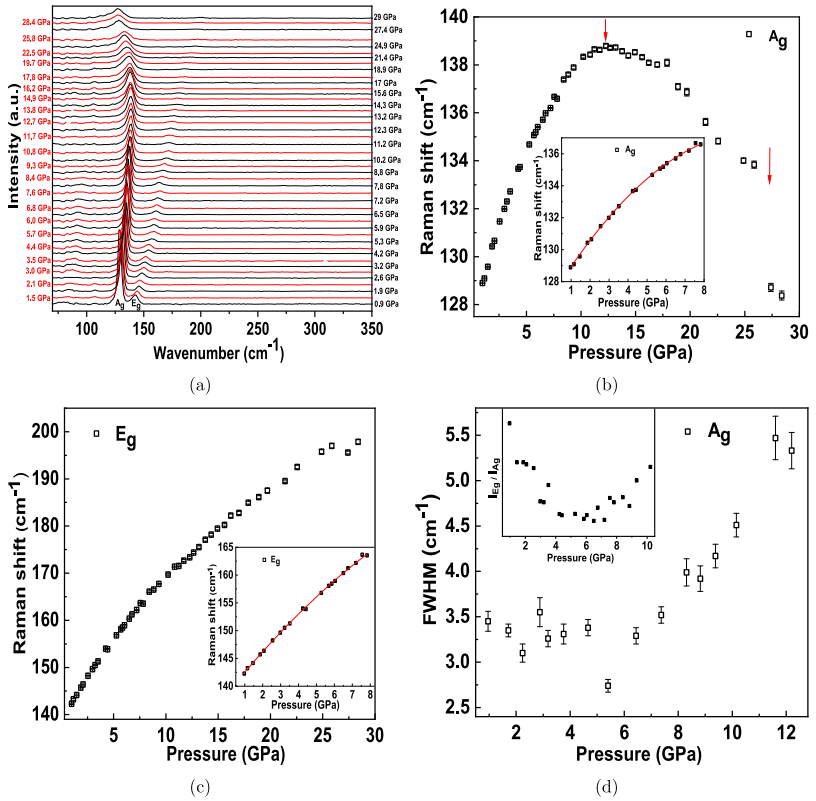

Figure 2. (a) Raman spectra of $TlInTe_2$ for various pressures at 298 K. The successive Raman spectra are represented as black and red colors. (b, c) Pressure dependence of A_g and E_g Raman modes. The quadratic fit to the frequency vs pressure of A_g and E_g modes are shown as the inset. The vertical arrows indicate different transitions. The size of the errors is smaller than the size of the symbols. (d) FWHM (cm^{-1}) vs pressure of A_g mode with error bars. FWHM (cm^{-1}) vs pressure of E_g mode with error bars. The intensity ratio of E_g and A_g modes with pressure is shown as an inset.

Figure 3b, c for comparison. The calculated static lattice constants are consistent with the HPXRD results at 298 K under high pressure. The pressure dependence of lattice parameter *a* seems to be steeper than that of *c*, which results from the anisotropic bonding nature of the $TlInTe_2$ lattice along the directions of the *a* and *c* crystallographic axes [Figures 3c and S4]. The anisotropic compression of *a* and *c* axes causes an obvious slope change in the lattice parameter ratio (c/a) versus pressure at 6 GPa, as shown in the inset of Figure 3d. Despite prominent changes noticed in the pressure-dependent phonon modes, the HPXRD study do not indicate any appreciable change at 25 GPa. In addition, the experimental EOS shows highly compressible lattice behavior compared to the theoretically obtained EOS. This is especially in the pressure range of 3−15 GPa, which is reflected from the low compressible nature of the lattice along the *c*-axis from the first-principles calculations. Overall, there is a good agreement between the theoretical and experimental EOS [Figure 3c]. To compute the equilibrium bulk modulus (B_0), we have fitted both experimental and calculated *P*−*V* data to the following third-order Birch−Murnaghan EOS (BM-EOS).[51]

$$P(V) = \frac{3B_0}{2}\left[\left(\frac{V_0}{V}\right)^{7/3} - \left(\frac{V_0}{V}\right)^{5/3}\right]\left\{1 + \frac{3}{4}(B_0' - 4)\left[\left(\frac{V_0}{V}\right)^{2/3} - 1\right]\right\} \quad (2)$$

where *P*, V_0, *V*, B_0, and B_0' are pressure, volume at zero pressure, deformed volume, equilibrium bulk modulus, and its first derivative, respectively. The calculated B_0 and its first derivative (B_0') determined from the experiment are 19.4 ± 1.2 and 7.30 ± 0.29 GPa, respectively. The calculated values of B_0 (25.55 GPa) and B_0' (5.08) from the theory is overestimated when compared to the experimental values, as shown in Figure 3c. The smaller bulk modulus value suggests a large compressibility of the $TlInTe_2$ lattice resulting from weaker bonding as discussed in the previous section.

Further to compliment our HP-Raman spectroscopy and XRD observations, first-principles CSP calculations have been performed independently at different pressures of ∼0, 10, 30, and 50 GPa with 2, 4, and 8 f.u. per primitive cell using the USPEX package.[38−40] The predicted crystal structure at ambient pressure is consistent with our experimental observation and also with the previous XRD measurements.[12] The ambient tetragonal structure is found to be stable up to 37.5 GPa, which is consistent with the present HP-XRD measurements. The B37 phase undergoes a pressure-induced structural phase transition to a body-centered cubic $Pm\bar{3}m$ (B2) phase at 50 GPa through an intermediate distorted orthorhombic (*Pbcm*) phase at 37.5 GPa. The predicted structural phase transition sequence in $TlInTe_2$ is analogous to that of parent structure of 1D chain materials such as TlSe and TlS[52] except the symmetry of the distorted intermediate phase [see Figures 4 and 5]. Interestingly, the B37 phase of $TlInTe_2$ exhibits structural stability relatively over wide pressure range (0−37.5 GPa) similar to TlS and TlSe. In contrast, InTe

https://doi.org/10.1021/acs.inorgchem.0c03795
Inorg. Chem. 2021, 60, 9320−9331

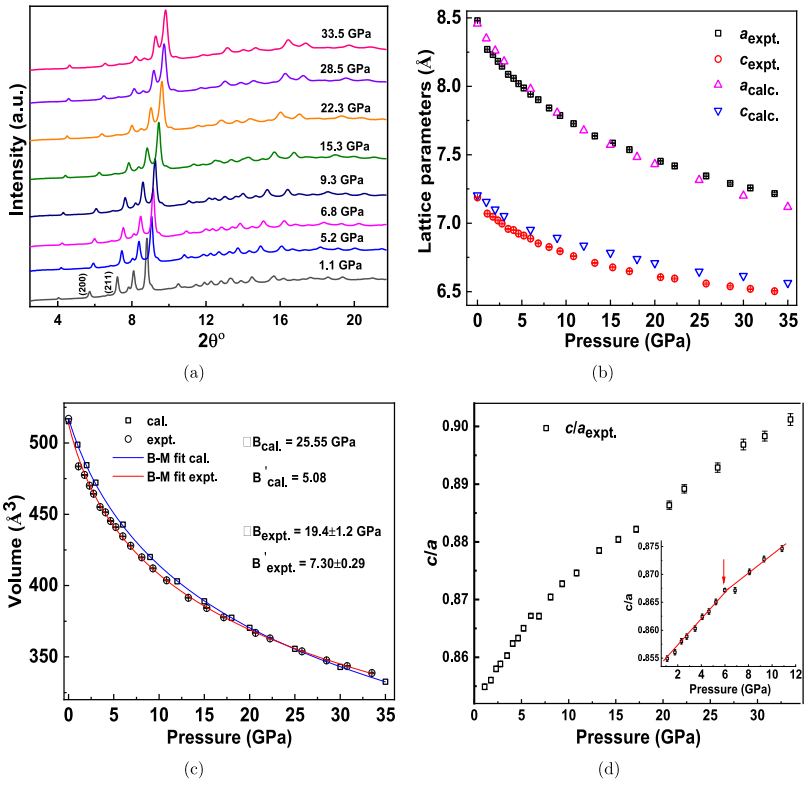

Figure 3. (a) Synchrotron XRD pattern of $TlInTe_2$ at selected pressures at 298 K. The Bragg peaks, (200) and (211), are indicated to show that their calculated intensities do not fit well with the observed intensity in Rietveld refinement; (b) lattice parameters vs pressure of $TlInTe_2$ from both HPXRD and first principles calculations; (c) EOS of $TlInTe_2$ is obtained by fitting the $P-V$ (HPXRD and first principles calculations) data to third-order BM-EOS. The size of the errors is smaller than the size of the symbols. (d) c/a ratio vs pressure of $TlInTe_2$ from the HPXRD. The line represents guidance to the eyes.

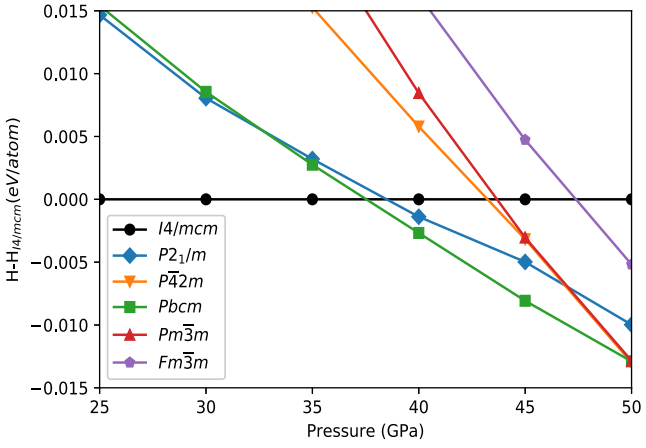

Figure 4. Calculated enthalpy difference of the predicted high-pressure phases relative to the ambient B37 phase as a function of pressure. The predicted structural transition sequence in $TlInTe_2$ is as follows: $I4/mcm \rightarrow Pbcm \rightarrow Pm\bar{3}m$ in the pressure range 0−50 GPa.

undergoes a series of structural phase transitions (B37 → B1 → B2) below 15 GPa.[25] The B37 (Z = 8) phase of InTe transforms to a sixfold coordinated B1 phase (Z = 4) at ∼ 6.5 GPa and with further compression, it transforms to eightfold coordinated B2 phase (Z = 4). In contrast to this, the B37 (Z = 4) phase of $TlInTe_2$ transforms to a distorted *Pbcm*-type structure, with further compression, it transforms to B2 (Z = 4) phase and might be to B1 (Z = 4) phase under very high pressure (see Figure 4). The fourfold In−Te_4 tetrahedra in B37 phase transforms to a distorted fourfold In−Te_4 tetrahedra with a *Pbcm*-type structure, which further transforms to an eightfold coordinated (In−Te_8 ordered polyhedra) B2 phase upon further compression. The *Pbcm*-type phase is a distorted structure of the B2 phase (see Figure 5). Overall, the common high-pressure B2 phase with eightfold coordination is observed for the iso-structural $TlInTe_2$, TlSe, TlS, and InTe compounds.[25,52] We also predicted metastable phases such as $P2_1/m$, $P\bar{4}2m$, and $Fm\bar{3}m$ (B1) at T = 0 K and they might be energetically competitive, if the kinetic effects are considered at high pressure. Thus, the predicted crystal structures provide very useful information on crystal structures of the TlSe family for future experimental and theoretical studies at high pressure. To explore the dynamical stability of the B37 phase, we computed phonon dispersion curves and projected density of states at ambient as well as at high pressure. The phonon profiles are well reproduced at ambient pressure.[12−14] The phonon frequencies are hardening and become more dispersive with pressure (see Figure S5). This clearly shows the dynamical stability of the B37 phase up to 30 GPa, which is consistent with our HP-XRD measurements. In addition, the unit cell parameters and atomic positions of the predicted B37 and high-pressure *Pbcm*-type and B2 phases are provided in Table S2 along with the available experimental data.[12]

High-Pressure Transport Measurements, Electronic Structure, and Fermi Surface Topology. As HPXRD studies do not exhibit any obvious signature of structural phase transitions corresponding to the phonon mode softening and a discontinuous change in the frequency of A_g mode at 10 and 25 GPa, respectively. The transport measurements were carried out to explore further details about the nature of transitions

https://doi.org/10.1021/acs.inorgchem.0c03795
Inorg. Chem. 2021, 60, 9320−9331

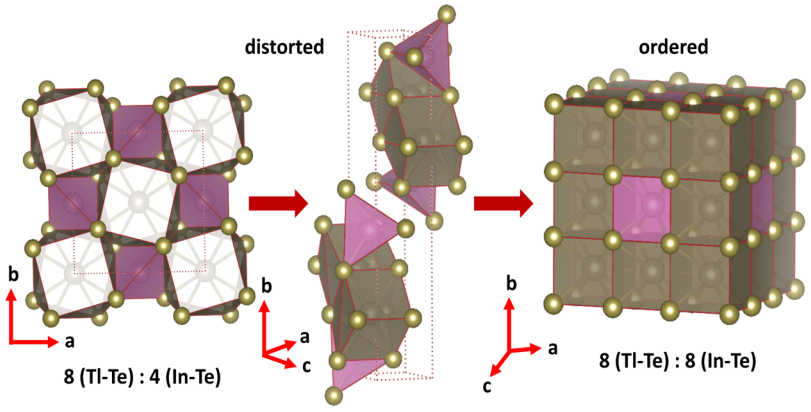

Figure 5. Crystal structures of predicted ambient *I*4/*mcm* (B37) (left), intermediate *Pbcm*-type (middle), and high-pressure $Pm\bar{3}m$ (B2) (right) phases of $TlInTe_2$.

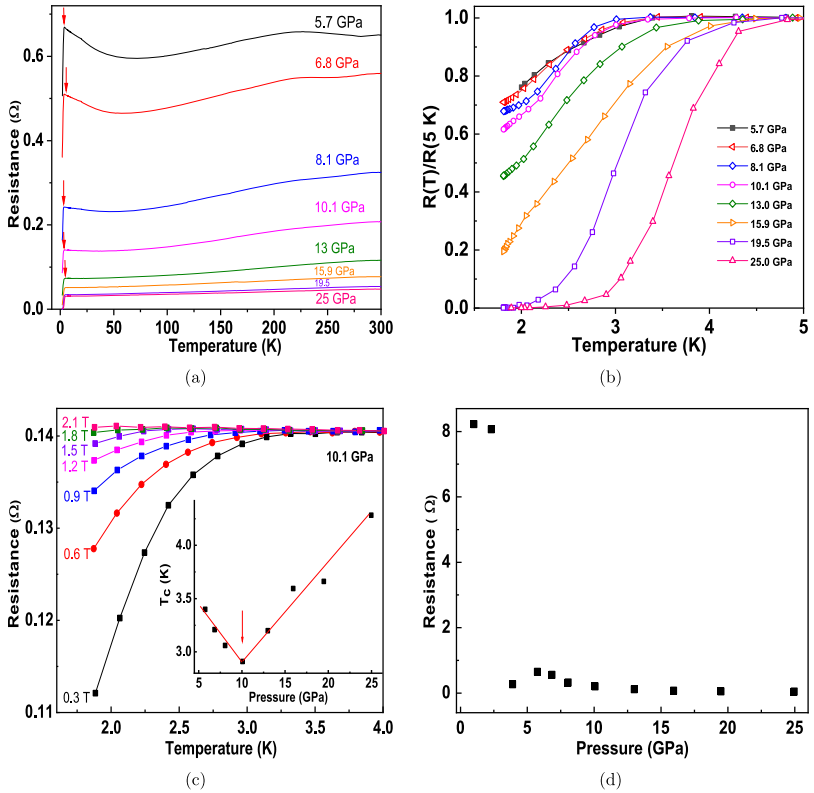

Figure 6. (a) Resistance vs temperature plot of $TlInTe_2$. The vertical red arrows at different pressures to show the T_c (b) normalized resistance vs temperature plot of $TlInTe_2$ for various pressures. (c) Resistance vs temperature for varying magnetic fields at 10.1 GPa of $TlInTe_2$ to confirm the superconducting transition. The critical superconducting transition temperature (T_c) vs resistance of $TlInTe_2$ is shown as an inset. The lines represent guidance to the eyes, and the vertical arrow is to show the V-shaped T_c behavior; (d) resistance vs temperature plot of $TlInTe_2$ at 298 K.

thus observed. Figure 6a shows resistance behavior of $TlInTe_2$ determined for selected pressures up to 3.9 GPa and temperatures down to 12 K, and to liquid He temperature for pressures at 5.7 GPa and above. The resistance behavior of $TlInTe_2$ measured at 1.1 GPa evinces a semiconducting behavior [see Figure 6a]. The resistance is suppressed with pressure and a dramatic decrease is observed at 3.9 GPa, resulting in semiconductor-to-semimetal transition.

Upon compression, the resistance drops to zero at 20 GPa, suggesting a superconducting transition. A constant resistance behavior is observed around 20 GPa. Our XRD and Raman data do not indicate any evidence of secondary phases, Te or InTe. So, we rule out the possibility of observed superconductivity from Te or InTe. Although the transport measurements were carried out under non-hydrostatic environment, the obtained results (observed anomalies) are unaltered except for a slight deviation from the transition pressures and these observations are supported by previous transport measurements under non-hydrostatic conditions on CdTe and ZnTe.[53] The observed transition pressure of the semiconductor-to-semimetal transition is in agreement with the single-crystal transport measurements on $TlInTe_2$ by Rabinal et al.[33] with quasi hydrostatic PTM. They observed saturation of parallel and perpendicular components of electrical resistivity at around 4 GPa is due to metallization. The critical temperature (T_c = 3.8 K) of the superconducting

https://doi.org/10.1021/acs.inorgchem.0c03795
Inorg. Chem. 2021, 60, 9320−9331

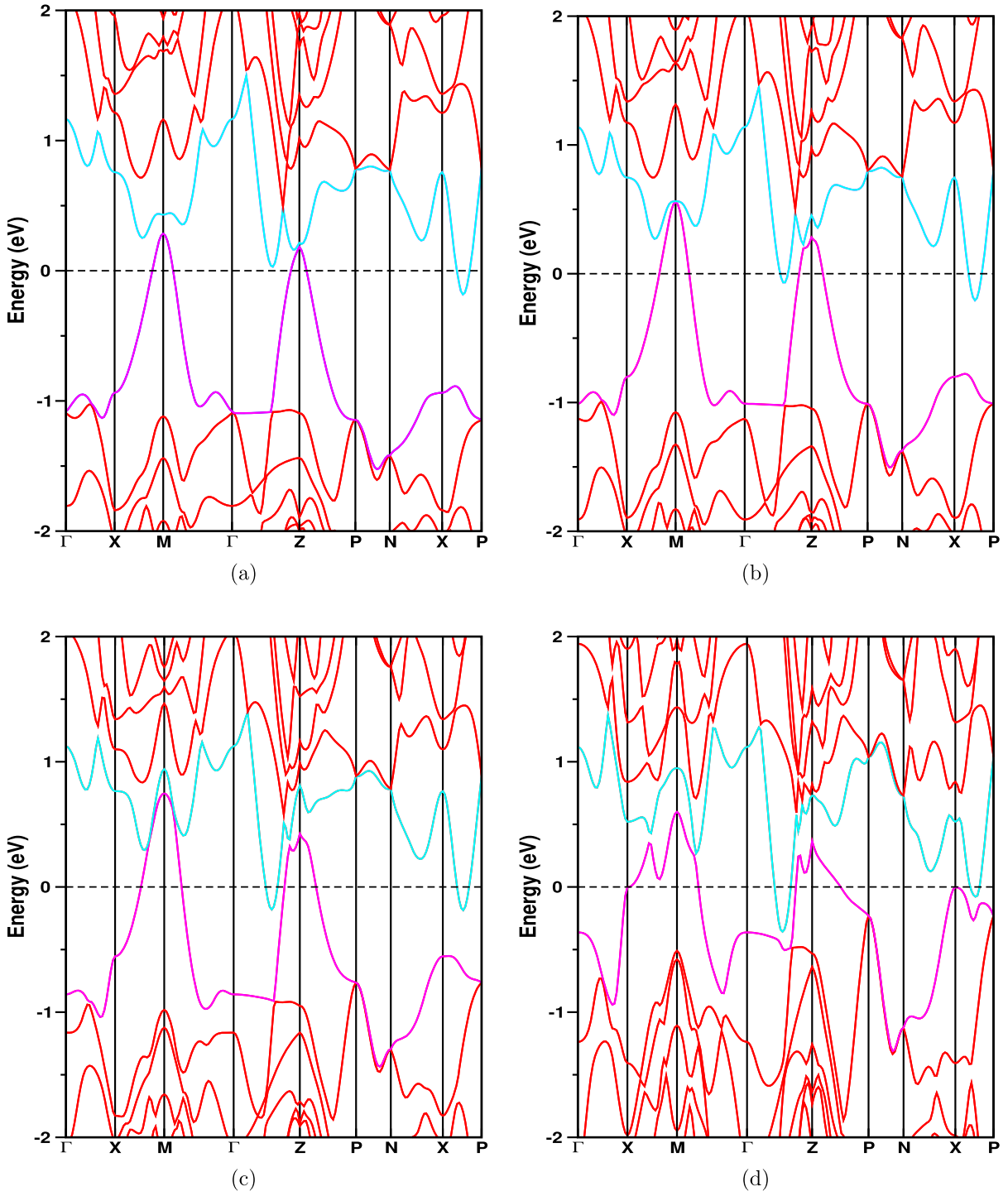

Figure 7. Calculated electronic band structure of B37 phase of $TlInTe_2$ for typical pressures (a) 6, (b) 9, (c) 15, and (d) 30 GPa with SOC.

transition is determined at 5.7 GPa. The smearing out of superconductivity under magnetic field for typical pressures at 5.7 and 10.1 GPa is shown in Figures 6c and S6, which confirms the presence of pressure-induced superconductivity in $TlInTe_2$. Figure 6c reveals magnetic field dependence of resistance at 10.1 GPa, and the superconductivity disappears completely at 2.1 T. The maximum T_c observed at ~ 25 GPa is 4.3 K. The procedure followed to calculate the T_c value from the resistance versus temperature plot is shown in Figure S6c. It is interesting to note the V-shaped T_c behavior of $TlInTe_2$ with the lowest T_c at 10 GPa, where giant softening of the A_g mode is also observed. More detailed experimental and theoretical[54] studies are required to confirm the above observations.

Electronic structure calculations were performed to obtain further insights on the above transitions and are discussed extensively in this section. The calculated electronic band structure of $TlInTe_2$ at ambient pressure reveals that it is an indirect band gap semiconductor with the top of valence band maximum (VBM) at the M point and the conduction band minimum (CBM) along $X-P$ high symmetry directions. At ambient pressure, the calculated electronic band gap without

https://doi.org/10.1021/acs.inorgchem.0c03795
Inorg. Chem. 2021, 60, 9320−9331

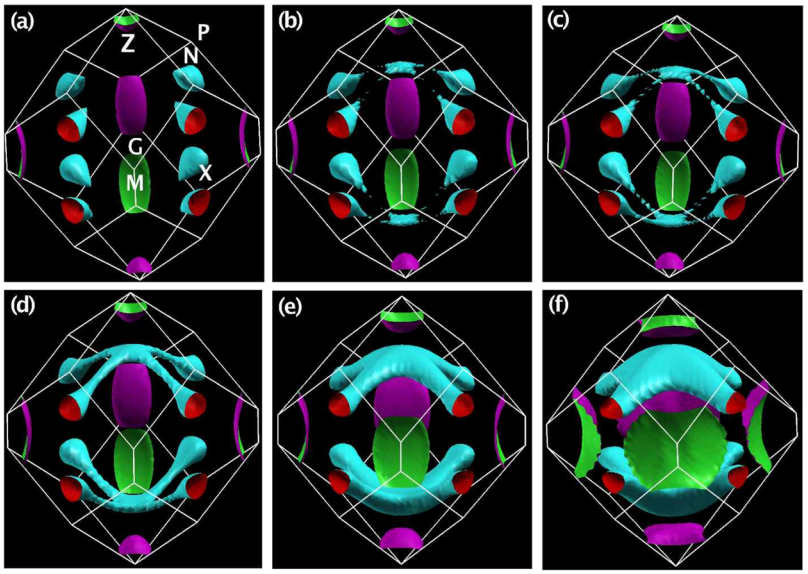

Figure 8. Calculated Fermi surface of B37 phase of $TlInTe_2$ at different pressures (a) 6.5, (b) 6.8, (c) 7, (d) 8, (e) 15, and (f) 30 GPa with SOC. New electron pockets are formed above 6.5 GPa and are strengthening with pressure. The new electron pockets are connecting with the other electron pockets in the form of tubular necks to form an (inverted) umbrella shaped Fermi surface in the first Brillouin zone over the studied pressure range.

(0.6 eV) and with (0.35 eV) SOC using TB-mBJ potential is shown in Figure S7. The obtained TB-mBJ band gap of 0.6 eV without SOC is consistent with the previously calculated band gap of 0.66 eV[55,56] but the TB-mBJ band gaps are improved over a PBE-GGA functional band gap of 0.12 eV.[12] However, the TB-mBJ band gap is still underestimated when compared to the experimentally observed optical band gap of 0.9−1.1 eV [ref 10 and refs therein] and previous theoretical band gap of 1.1 eV is obtained using the HSE06 functional without SOC.[47] The computed partial density of states (PDOS) of $TlInTe_2$ at ambient pressure is shown in Figure S8a. It can be inferred from Figure S8 that the top of the valence band is mainly dominated by Te 5p states and Tl 6s states and they are weakly hybridized with each other. The weak 5p electron hybridization of Te atoms and almost isolated 6s electronic distribution around Tl atoms impose a moderate constraint on the movement of Tl atoms, resulting in a strong dynamic abnormality (anharmonicity) in this material.[47] The minimum of the conduction band is mainly derived from the In 5s, Te 5p, and Tl 6p states. In general, the states near the Fermi level contribute to the electron−hole transport mechanism from CBM and VBM, respectively. The intrinsic multi-valley degeneracy at *Z* and along *X*−*P* directions at the CBM and along *M* and *Z* at VBM is favorable for an efficient electronic transport mechanism and is not intrinsic in commercially available thermoelectric materials, Bi_2Te_3 and PbTe.[13] Under high pressure, the 5p (Te) and 6s (Tl)-states from the valence band (at *M* and *Z* point of the Brillouin zone) and 5s-states of In from the conduction band (along *X*−*P* direction of Brillouin zone) do cross the Fermi level leading to semiconductor → semi metal transition around 6 GPa (see Figure S9) and it becomes metal upon further compression above 20 GPa due to delocalization or dispersive nature of the bands around the Fermi level, as illustrated in Figures 7, 8, and S9. However, $TlInSe_2$ becomes (semi)metal with and without SOC around 20 and up to 30 GPa, respectively. SOC plays a significant role during metallization for $TlInSe_2$ under pressure.[9]

A possibility of the topological nontrivial phase has already been predicted for TlSe family. For instance, the first-principles calculations on monolayer TlSe reveals an occurrence of topological crystalline insulator state at ambient pressure, which transforms to a topological insulating state under tensile strain.[24] Similarly, InTe from the same family is predicted to exhibit two successive band inversions at *Z* and *M* point of the Brillouin zone at ∼1 and ∼1.4 GPa, respectively.[25] A comparison of band structures of $TlInTe_2$ and InTe suggests that the presence of Tl 6s-states near the Fermi level completely changes the band topology of $TlInTe_2$ when compared to InTe. In addition, the electronic band structure calculations reveal that the applied pressure simultaneously increases electron and hole populations in the B37 phase (see Figure 7), as reported for InTe[25] and $NbAs_2$.[26]

The increase in FWHM (cm^{-1}) of the A_g phonon mode frequency at 6 GPa might be attributed to the change in topology of the Fermi surface. In order to obtain deeper insights into the origin of superconductivity, we carried out a detailed analysis of changes in the Fermi surface topology as a function of pressure. Lifshitz transition is an electronic topological transition of the Fermi surface without change in its crystal symmetry, and it can occur through changing external parameters such as chemical doping, pressure, temperature, magnetic field, and so forth. The changes in the topology of the Fermi surface of bulk crystals are explained by Lifshitz in four possible ways.[57,58] (1) The creation or (2) disappearance of a pocket in the Fermi surface (Lifshitz transition of L1 type); (3) creation or (4) disappearance of a neck in the Fermi surface (so called Lifshitz neck disruption transition of the L2 type). As illustrated in Figure 8, the calculated Fermi surface at 6 (semiconductor to semimetal transition) and 6.5 GPa (see Figure 8a) show individual hole (magenta) and electron (cyan) pockets. Above 6.5 GPa, the electron pockets are connected through newly emerged spots in the Fermi surface (see Figure 8b, c). The connectivity of the electron pockets strengthening as a function of pressure, along with the appearance of new spots on the Fermi surface. The

https://doi.org/10.1021/acs.inorgchem.0c03795
Inorg. Chem. 2021, 60, 9320−9331

appearance of new spots and the connecting points of the electron pockets grow as tubular necks, forming an (inverted) umbrella-shaped Fermi surface within the first Brillouin zone, which are ascribed to L1- and L2-type Lifshitz transitions, respectively, in the pressure range of 6.5−8 GPa. Therefore, the combination of L1- and L2-type transitions might be responsible for the emergence of superconductivity in the B37 phase of $TlInTe_2$ as observed in our transport measurements at 5.7 GPa. Analogous to $TlInTe_2$, pressure-induced Fermi surface topology change (Lifshitz transition) is reported for quasi-2D ZrSiTe,[28] ThFeAsN,[27] SnSe,[29,30] and bulk H_3S.[31]

To discern the frequency reversal of the A_g phonon mode around 12 GPa, we carried out a detailed line shape analysis of phonon modes. Surprisingly, an obvious asymmetry begins to emerge at P = 8.8 GPa and above to the left (low frequency region) of the A_g mode. This asymmetry could not be fitted well with a pure Lorentzian, but it could fit very well with a Fano line shape function, as shown in Figure S10. The Fano asymmetry in phonon line shape arises as a result of coherent coupling of Fano interference between discrete phononic states with the broad electronic continuum formed by the conduction electrons. The asymmetric line shape observed in the A_g phonon mode is fitted with the Fano line shape using the following equation[59,60]

$$I(\omega) = A\frac{(q+\epsilon)^2}{1+\epsilon^2}; \qquad \text{where } \epsilon = \frac{\omega-\omega_0}{\Gamma} \tag{3}$$

where A is a constant, ω_0 is the modified (re-normalized) frequency in the presence of electron−phonon interaction, q is the asymmetric parameter, $1/q$ is the strength of the interaction, and Γ (cm^{-1}) is the phonon line width, which is related to the phonon lifetime. As $1/q$ tends to zero, the Fano line shape becomes Lorentzian. Figure S10 represents the fitting of A_g phonon mode with eq 3, yielding q = −10.84(1.00) and Γ = 2.10(0.5) cm^{-1}. A negative q value represents the interference between discrete phonon states with the electron continuum of the conduction electrons constructively at the lower frequency (cm^{-1}) region, whereas it destructively interferes at the higher frequency (cm^{-1}) region. The large asymmetric parameter (q) values suggests that the electron−phonon interaction strength is weak. The pressure dependence of q exhibits a maximum around 10.5 GPa. Thus, the giant phonon frequency softening and change in asymmetry parameter changes suggest a prominent electron−phonon coupling in $TlInTe_2$ above 8 GPa at room temperature. A phonon mode softening similar to that reported here for $TlInTe_2$ has already been observed in cuprate and yttrium barium copper oxide ($YbBa_2Cu_3O_7$) at low temperatures, which is attributed to the electron−phonon coupling.[61,62] As illustrated in Figure S8, the conduction electrons are contributed prominently by In 5s, Tl 6p, and Te 5p orbitals at 15 GPa. Recent theoretical work[54] reproduces the superconductivity and V-shaped T_c behavior based on the interplay between the observed optical phonon energy (ω_0) and anharmonic damping (Γ) from the Raman scattering measurements of this work. Based on these two parameters, they proposed variation of T_c with pressure in two regions, that is, coherent (where phonons behave like quasi particles) and non-coherent regions (where phonons behave like diffusions). The degree of coherence ($D = \Gamma/\omega_0$ for $TlInTe_2$ is found to be far less than 1, *i.e.* $\Gamma \ll \omega_0$ belongs to coherent region, where T_c is decreasing with increasing ω_0 and reaches to a minimum value at which ω_0 is maximum and then raising with decreasing ω_0 above 10 GPa which leads to a Stokes/anti-Stokes constructive interference in the presence of anharmonic damping which enhances the Cooper pairing. In addition, the observed giant phonon softening of A_g phonon mode guided to explain V-shaped T_c behavior under pressure for $TlInTe_2$. The frequency reversal of the A_g phonon mode and its increase in linewidth can also be related to the pressure induced anharmonic effects of phonon modes.

Finally, we explore the plausible reasons for the origin of ∼4% discontinuous frequency change of A_g phonon mode and also a subtle frequency change of E_g mode at ∼25 GPa. The HPXRD studies and DFT calculations reveal that the frequency discontinuity is not accompanied by changes in any of the structural parameters, unit cell volume, lattice parameters and coordination numbers. Since we could not extract bond lengths and bond angles from HPXRD data, we have calculated bond parameters from the first-principles calculations. Interestingly, we have noticed that the In−Te bond length stiffen above 25 GPa, as shown in Figure S11. Similarly, a subtle slope change is also noticed in the bond lengths of In−In and Tl−Tl [Figure S11]. Hence, the origin of frequency discontinuity cannot be explained by the bond length stiffening occurring at 25 GPa. As shown in Figure S12, we observed discontinuities in the calculated in-equivalent bond angles (Te−Tl−Te) of distorted Thomson cube of $Tl-Te_8$ at 5−6 and 10−12 GPa. The first discontinuity in the pressure range of 5−6 GPa is due to semiconductor-to-semimetal transition, and the second discontinuity is accompanied with the giant A_g phonon mode softening at 10−12 GPa. Pressure dependence of bond angles do not provide any evidence of drastic change seen at 25 GPa. So, we carried out a detailed structural analysis to ascertain, if the discontinuous change in the A_g phonon frequency is induced by changes in dimensionality or tilting of the $Tl-Te_8$ Thomson cube. As illustrated in Figure 5, the 1D nature of the ambient B37 phase remains robust even up to 37.5 GPa and a continuous rotation of square planes of Thompson cubes induces a systematic tilting (see Figure S13). However, the continuous tilting does not justify an abrupt frequency change at 25 GPa. Hence, we rule out the possibility of either 1D (chains) to 2D (sheets/planes) or tilting of $Tl-Te_8$ changes as driving force for the observed frequency change at 25 GPa. We anticipate that the plausible origin of the frequency discontinuity at 25 GPa might be stemmed from some other unknown phenomena, and more detailed studies are required to resolve its origin.

CONCLUSIONS

The structural, vibrational, and electronic properties of $TlInTe_2$ compound has been investigated using high-pressure Raman spectroscopy, synchrotron XRD, transport measurements, and first-principles CSP calculations. A semiconductor-to-semimetal transition is observed around 4 GPa followed by a superconducting transition at 5.7 GPa with a T_c of 3.8 K. A giant A_g phonon mode softening observed at 10−12 GPa is ascribed to the interaction between the discrete phonon states with electronic continuum of conduction electrons from the In 5s or Te 5p (or both) conduction electrons causing Fano line shape in the A_g mode due to electron−phonon coupling. The CSP calculations predicted two high-pressure phases above 35 GPa resulting in the structural phase transition sequence as; B37 → *Pbcm* → B2 under high pressure. Electronic structure

https://doi.org/10.1021/acs.inorgchem.0c03795
Inorg. Chem. 2021, 60, 9320−9331

calculations suggest Lifshitz transitions near superconducting transition pressure. Finally, a plausible origin of ∼4% discontinuous frequency change of the A_g phonon mode coupled with In−Te and Tl−Tl/In−In bond length changes at 25 GPa is yet to be resolved. Our study provide a new direction to unveil unprecedented pressure-induced novel phenomena in the TlSe family.

■ ASSOCIATED CONTENT

Supporting Information

The Supporting Information is available free of charge at https://pubs.acs.org/doi/10.1021/acs.inorgchem.0c03795.

Observed Raman frequencies and predicted structural parameters of ambient and high-pressure phases, Raman spectra, Le Bail fitting, Rietveld refinement, normalized lattice constants, phonon dispersions and DOS, resistance−temperature, electronic band structure at ambient pressure, band gap as a function of pressure, electronic density of states at high pressure, Lorentzian and Fano line shapes of A_g mode, calculated bond lengths and angles, and crystal structure of the ambient phase at different pressures (PDF)

■ AUTHOR INFORMATION

Corresponding Authors

Sorb Yesudhas − *Center for High-Pressure Science & Technology Advanced Research, Beijing 100094, P. R. China*; Email: sorubya@gmail.com

N. Yedukondalu − *Department of Geosciences, Center for Materials by Design, and Institute for Advanced Computational Science, State University of New York, Stony Brook, New York 11794, United States; Joint Photon Sciences Institute, Earth and Space Science Building, Stony Brook University, Stony Brook, New York 11794, United States; Rajiv Gandhi University of Knowledge Technologies, Basar, Telangana 504107, India*; orcid.org/0000-0002-7650-7567; Email: nykondalu@gmail.com

Yang Ding − *Center for High-Pressure Science & Technology Advanced Research, Beijing 100094, P. R. China*; Email: yang.ding@hpstar.ac.cn

Authors

Manoj K. Jana − *New Chemistry Unit, Jawaharlal Nehru Centre for Advanced Scientific Research (JNCASR), Bangalore 560064, India*; orcid.org/0000-0001-9128-2493

Jianbo Zhang − *Center for High-Pressure Science & Technology Advanced Research, Beijing 100094, P. R. China*; orcid.org/0000-0002-8339-1099

Jie Huang − *Center for High-Pressure Science & Technology Advanced Research, Beijing 100094, P. R. China*

Bijuan Chen − *Center for High-Pressure Science & Technology Advanced Research, Beijing 100094, P. R. China*

Hongshang Deng − *Center for High-Pressure Science & Technology Advanced Research, Beijing 100094, P. R. China*; orcid.org/0000-0002-6871-2739

Raimundas Sereika − *Center for High-Pressure Science & Technology Advanced Research, Beijing 100094, P. R. China; Vytautas Magnus University, Kaunas 44248, Lithuania*

Hong Xiao − *Center for High-Pressure Science & Technology Advanced Research, Beijing 100094, P. R. China*; orcid.org/0000-0001-8859-9967

Stanislav Sinogeikin − *DAC Tools, Custom Equipment for High-Pressure Research, Naperville, Illinois 60565-2925, United States*

Curtis Kenney-Benson − *HPCAT, X-ray Science Division, Advanced Photon Source, Argonne National Laboratory, Lemont, Illinois 60439, United States*

Kanishka Biswas − *New Chemistry Unit, Jawaharlal Nehru Centre for Advanced Scientific Research (JNCASR), Bangalore 560064, India*; orcid.org/0000-0001-9119-2455

John B. Parise − *Department of Geosciences, Center for Materials by Design, and Institute for Advanced Computational Science, State University of New York, Stony Brook, New York 11794, United States; National Synchrotron Light Source II, Brookhaven National Laboratory, Upton, New York 11973, United States; Joint Photon Sciences Institute, Earth and Space Science Building, Stony Brook University, Stony Brook, New York 11794, United States*

Ho-kwang Mao − *Center for High-Pressure Science & Technology Advanced Research, Beijing 100094, P. R. China*

Complete contact information is available at: https://pubs.acs.org/10.1021/acs.inorgchem.0c03795

Notes

The authors declare no competing financial interest.

■ ACKNOWLEDGMENTS

Y.D. acknowledges the support from National Key Research and Development Program of China 2018YFA0305703; the National Natural Science Foundation of China (NSFC)-U1930401, 11874075, and Science Challenge Project TZ2016001. HPXRD studies were performed at HPCAT (Sector 16), Advanced Photon Source (APS), Argonne National Laboratory. HPCAT operations are supported by DOE-NNSA's Office of Experimental Sciences. The APS is a U.S. Department of Energy (DOE) Office of Science User Facility operated for the DOE Office of Science by Argonne National Laboratory under contract no. DE-AC02-06CH11357. We acknowledge Sergey Tkachev, GSECARS, APS, for Ne gas loading in the DAC. N.Y. would like to thank the Science and Engineering Research Board and Indo-US Scientific Technology Forum and National Science Foundation (EAR-1723160) for funding. N.Y. would like to acknowledge Prof. Artem R. Oganov (supervisor) and Dr. M. Mahdi Davari Esfahani for their support and discussions and also Institute for Advanced Computational Science, Stony Brook University, for providing computational resources (Seawulf cluster). YAS acknowledges HPSTAR for post-doctoral fellowship. K.B. acknowledges Sheikh Saqr Career Fellowship and Department of Science & Technology, India, for partial support.

■ REFERENCES

(1) Zhang, J. L.; Zhang, S. J.; Weng, H. M.; Zhang, W.; Yang, L. X.; Liu, Q. Q.; Feng, S. M.; Wang, X. C.; Yu, R. C.; Cao, L. Z.; et al. Pressure-induced superconductivity in topological parent compound Bi_2Te_3. *Proc. Natl. Acad. Sci. U.S.A.* **2011**, *108*, 24−28.

(2) Kung, H.-H.; Goyal, A. P.; Maslov, D. L.; Wang, X.; Lee, A.; Kemper, A. F.; Cheong, S.-W.; Blumberg, G. Observation of chiral surface excitons in a topological insulator Bi_2Te_3. *Proc. Natl. Acad. Sci. U.S.A.* **2019**, *116*, 4006−4011.

(3) Zhu, L.; Wang, H.; Wang, Y.; Lv, J.; Ma, Y.; Cui, Q.; Ma, Y.; Zou, G. Substitutional alloy of Bi and Te at high pressure. *Phys. Rev. Lett.* **2011**, *106*, 145501.
(4) Sorb, Y. A.; Rajaji, V.; Malavi, P. S.; Subbarao, U.; Halappa, P.; Peter, S. C.; Karmakar, S.; Narayana, C. Pressure-induced electronic topological transition in Sb_2S_3. *J. Phys.: Condens. Matter* **2015**, *28*, 015602.
(5) Jabarov, S. H.; Ismayilova, N. A.; Kozlenko, D. P.; Mammadov, T. G.; Mamedov, N. T.; Orudzhev, H. S.; Kichanov, S. E.; Mikailzade, F. A.; Kasumova, E. K.; Dang, N. T. Structural and elastic properties of $TlInSe_2$ at high pressure. *Solid State Sci.* **2021**, *111*, 106343.
(6) Mamedov, N. T.; Jabarov, S. H.; Kozlenko, D. P.; Ismayilova, N. A.; Seyidov, M. Y.; Mammadov, T. G.; Dang, N. T. Neutron diffraction study of the crystal structure of $TlInSe_2$ at high pressure. *Int. J. Mod. Phys. B* **2019**, *33*, 1950149.
(7) Dutta, M.; Samanta, M.; Ghosh, T.; Voneshen, D. J.; Biswas, K. Evidence of Highly Anharmonic Soft Lattice Vibrations in a Zintl Rattler. *Angew. Chem., Int. Ed.* **2021**, *60*, 4259−4265.
(8) Dutta, M.; Matteppanavar, S.; Prasad, M. V. D.; Pandey, J.; Warankar, A.; Mandal, P.; Soni, A.; Waghmare, U. V.; Biswas, K. Ultralow Thermal Conductivity in Chain Like TlSe due to Inherent Tl^+ Rattling. *J. Am. Chem. Soc.* **2019**, *141*, 20293−20299.
(9) Ghafari, A.; Habicht, K. Electronic structure and transport properties of $TlInSe_2$ and $Tl_{05}Li_{05}InSe_2$. *Mater. Today Energy* **2019**, *12*, 95−106.
(10) Panich, A. M. Electronic properties and phase transitions in low-dimensional semiconductors. *J. Phys.: Condens. Matter* **2008**, *20*, 293202.
(11) Mamedov, N.; Wakita, K.; Ashida, A.; Matsui, T.; Morii, K. Super thermoelectric power of one-dimensional $TlInSe_2$. *Thin Solid Films* **2006**, *499*, 275−278.
(12) Jana, M. K.; Pal, K.; Warankar, A.; Mandal, P.; Waghmare, U. V.; Biswas, K. Intrinsic rattler-induced low thermal conductivity in Zintl-type $TlInTe_2$. *J. Am. Chem. Soc.* **2017**, *139*, 4350−4353.
(13) Ding, G.; He, J.; Cheng, Z.; Wang, X.; Li, S. Low lattice thermal conductivity and promising thermoelectric figure of merit of Zintl type $TlInTe_2$. *J. Mater. Chem. C* **2018**, *6*, 13269−13274.
(14) Pal, K.; Xia, Y.; Wolverton, C. Microscopic mechanism of unusual lattice thermal transport in $TlInTe_2$. *npj Comput. Mater.* **2021**, *7*, 5.
(15) Ellialtıoğlu, Ş.; Mete, E.; Shaltaf, R.; Allakhverdiev, K.; Gashimzade, F.; Nizametdinova, M.; Orudzhev, G. Electronic structure of the chainlike compound TlSe. *Phys. Rev. B: Condens. Matter Mater. Phys.* **2004**, *70*, 195118.
(16) Müller, D.; Eulenberger, G.; Hahn, H. Über ternäre Thalliumchalkogenide mit Thalliumselenidstruktur. *Z. Anorg. Allg. Chem.* **1973**, *398*, 207−220.
(17) Zevalkink, A.; Toberer, E. S.; Zeier, W. G.; Flage-Larsen, E.; Snyder, G. J. Ca_3AlSb_3: an inexpensive, non-toxic thermoelectric material for waste heat recovery. *Energy Environ. Sci.* **2011**, *4*, 510−518.
(18) Toberer, E. S.; Zevalkink, A.; Crisosto, N.; Snyder, G. J. The Zintl compound $Ca_5Al_2Sb_6$ for low-cost thermoelectric power generation. *Adv. Funct. Mater.* **2010**, *20*, 4375−4380.
(19) Ebnalwaled, A. A.; Al-Orainy, R. H. Anisotropic properties and conduction mechanism of $TlInSe_2$ chain semiconductor. *Appl. Phys. A* **2013**, *112*, 955−961.
(20) Abdullaev, F. N.; Kerimova, T. G.; Abdullaev, N. A. Conductivity anisotropy and localization of charge carriers in $TlInTe_2$ single crystals. *Phys. Solid State* **2005**, *47*, 1221−1224.
(21) Sorb, Y. A.; Subramanian, N.; Ravindran, T. R. High pressure Raman spectroscopy of layered matlockite, PbFCl. *J. Phys.: Condens. Matter* **2013**, *25*, 155401.
(22) Yedukondalu, N.; Davari Esfahani, M. M. Unraveling the Hidden Martensitic Phase Transition in BaClF and PbClF under High Pressure Using an Ab Initio Evolutionary Approach. *Inorg. Chem.* **2019**, *58*, 5886−5899.
(23) Geller, S.; Jayaraman, A.; Hull, G. W., Jr. Superconductivity and vacancy structures of the pressure-induced NaCl-type phases of the In-Te system. *Appl. Phys. Lett.* **1964**, *4*, 35−37.
(24) Niu, C.; Buhl, P. M.; Bihlmayer, G.; Wortmann, D.; Blügel, S.; Mokrousov, Y. Two-dimensional topological crystalline insulator and topological phase transition in TlSe and TlS monolayers. *Nano Lett.* **2015**, *15*, 6071−6075.
(25) Rajaji, V.; Pal, K.; Sarma, S. C.; Joseph, B.; Peter, S. C.; Waghmare, U. V.; Narayana, C. Pressure induced band inversion, electronic and structural phase transitions in InTe: A combined experimental and theoretical study. *Phys. Rev. B* **2018**, *97*, 155158.
(26) Li, Y.; An, C.; Hua, C.; Chen, X.; Zhou, Y.; Zhou, Y.; Zhang, R.; Park, C.; Wang, Z.; Lu, Y.; et al. Pressure-induced superconductivity in topological semimetal $NbAs_2$. *npj Quantum Mater.* **2018**, *3*, 58.
(27) Sen, S.; Guo, G.-Y. Pressure induced Lifshitz transition in ThFeAsN. *Phys. Rev. Mater.* **2020**, *4*, 104802.
(28) Krottenmüller, M.; Vöst, M.; Unglert, N.; Ebad-Allah, J.; Eickerling, G.; Volkmer, D.; Hu, J.; Zhu, Y. L.; Mao, Z. Q.; Scherer, W.; et al. Indications for Lifshitz transitions in the nodal-line semimetal ZrSiTe induced by interlayer interaction. *Phys. Rev. B* **2020**, *101*, No. 081108(R).
(29) Biesner, T.; Li, W.; Tsirlin, A. A.; Roh, S.; Wei, P.-C.; Uykur, E.; Dressel, M. Spectroscopic trace of the Lifshitz transition and multivalley activation in thermoelectric SnSe under high pressure. *NPG Asia Mater.* **2021**, *13*, 12.
(30) Nishimura, T.; Sakai, H.; Mori, H.; Akiba, K.; Usui, H.; Ochi, M.; Kuroki, K.; Miyake, A.; Tokunaga, M.; Uwatoko, Y.; et al. Large Enhancement of Thermoelectric Efficiency Due to a Pressure-Induced Lifshitz Transition in SnSe. *Phys. Rev. Lett.* **2019**, *122*, 226601.
(31) Bianconi, A.; Jarlborg, T. Superconductivity above the lowest Earth temperature in pressurized sulfur hydride. *Europhys. Lett.* **2015**, *112*, 37001.
(32) Ves, S. High Pressure Raman Study of the "Chain" Chalcogenide $TlInTe_2$. *Phys. Status Solidi B* **1990**, *159*, 699−706.
(33) Rabinal, M. K.; Titus, S. S. K.; Asokan, S.; Gopal, E. S. R.; Godzaev, M. O.; Mamedov, N. T. Effect of High Pressure on the Electrical Conductivity of $TlInX_2$ (X= Se, Te) Layered Semiconductors. *Phys. Status Solidi B* **1993**, *178*, 403−408.
(34) Klotz, S.; Chervin, J.-C.; Munsch, P.; Le Marchand, G. Hydrostatic limits of 11 pressure transmitting media. *J. Phys. D: Appl. Phys.* **2009**, *42*, 075413.
(35) Hammersley, A. P.; Svensson, S. O.; Hanfland, M.; Fitch, A. N.; Hausermann, D. Two-dimensional detector software: from real detector to idealised image or two-theta scan. *Int.J. High Pres. Res.* **1996**, *14*, 235−248.
(36) Rodríguez-Carvajal, J. Recent advances in magnetic structure determination by neutron powder diffraction. *Phys. B* **1993**, *192*, 55−69.
(37) Mao, H. K.; Bell, P. M. High-pressure physics: the 1-megabar mark on the ruby R1 static pressure scale. *Science* **1976**, *191*, 851−852.
(38) Oganov, A. R.; Glass, C. W. Crystal structure prediction using ab initio evolutionary techniques: Principles and applications. *J. Chem. Phys.* **2006**, *124*, 244704.
(39) Lyakhov, A. O.; Oganov, A. R.; Stokes, H. T.; Zhu, Q. New developments in evolutionary structure prediction algorithm USPEX. *Comput. Phys. Commun.* **2013**, *184*, 1172−1182.
(40) Oganov, A. R.; Lyakhov, A. O.; Valle, M. How Evolutionary Crystal Structure Prediction Works—and Why. *Acc. Chem. Res.* **2011**, *44*, 227−237.
(41) Kresse, G.; Joubert, D. From ultrasoft pseudopotentials to the projector augmented-wave method. *Phys. Rev. B: Condens. Matter Mater. Phys.* **1999**, *59*, 1758−1775.
(42) Perdew, J. P.; Burke, K.; Ernzerhof, M. Generalized Gradient Approximation Made Simple. *Phys. Rev. Lett.* **1996**, *77*, 3865−3868.
(43) Kresse, G.; Furthmüller, J. Efficient iterative schemes for ab initio total-energy calculations using a plane-wave basis set. *Phys. Rev. B: Condens. Matter Mater. Phys.* **1996**, *54*, 11169−11186.

https://doi.org/10.1021/acs.inorgchem.0c03795
Inorg. Chem. 2021, 60, 9320−9331

(44) Tran, F.; Blaha, P. Accurate Band Gaps of Semiconductors and Insulators with a Semilocal Exchange-Correlation Potential. *Phys. Rev. Lett.* **2009**, *102*, 226401.
(45) Schwarz, K.; Blaha, B.; Madsen, G. K. H. Electronic structure calculations of solids using the WIEN2k package for material sciences. *Comput. Phys. Commun.* **2002**, *147*, 71−76. Proceedings of the Europhysics Conference on Computational Physics Computational Modeling and Simulation of Complex Systems
(46) Gasanly, N. M.; Goncharov, A. F.; Dzhavadov, B. M.; Melnik, N. N.; Tagirov, V. I.; Vinogradov, E. A. Vibrational spectra of $TlGaTe_2$, $TlInTe_2$, and $TlInSe_2$ layer single crystals. *Phys. Status Solidi B* **1980**, *97*, 367−377.
(47) Wu, M.; Khan, E.; Huang, L. Unusual lattice thermal conductivity in the simple crystalline compounds $TlXTe_2$ (X = Ga, In). *Phys. Rev. B* **2019**, *100*, 075207.
(48) Alekperov, O. Z.; Nakhmedov, E.; Najafov, A.; Samedov, O.; Nadirova, K.; Gasymov, V.; Mahmudova, G. R. Reversible amorphization under ac electric field and character of conductivity of $TlInTe_2$ crystal at ionic conductivity temperature. *J. Phys. D: Appl. Phys.* **2019**, *53*, 035103.
(49) Mimura, K.; Hosokawa, S.; Happo, N.; Hu, W.; Hayashi, K.; Wakita, K.; Ishii, H.; Yoshimura, M.; Jeyakanthan, J.; Mamedov, N. Three Dimensional Atomic Image of $TlInSe_2$ by X-ray Fluorescence Holography. *e-J. Surf. Sci. Nanotechnol.* **2011**, *9*, 273−276.
(50) Hosokawa, S.; Kamimura, K.; Ikemoto, H.; Happo, N.; Mimura, K.; Hayashi, K.; Takahashi, K.; Wakita, K.; Mamedov, N. Structural studies on $TlInSe_2$ thermoelectric material by X-ray fluorescence holography, XAFS, and X-ray diffraction. *Phys. Status Solidi B* **2015**, *252*, 1225−1229.
(51) Birch, F. Finite Elastic Strain of Cubic Crystals. *Phys. Rev.* **1947**, *71*, 809−824.
(52) Demishev, G. B.; Kabalkina, S. S.; Kolobyanina, T. N. X-ray studies of thallium chalcogenides TIS and TISe up to 37 GPa. *Phys. Status Solidi A* **1988**, *108*, 89−95.
(53) Errandonea, D.; Segura, A.; Martínez-García, D.; Muñoz-San Jose, V. Hall-effect and resistivity measurements in CdTe and ZnTe at high pressure: Electronic structure of impurities in the zinc-blende phase and the semimetallic or metallic character of the high-pressure phases. *Phys. Rev. B: Condens. Matter Mater. Phys.* **2009**, *79*, 125203.
(54) Setty, C.; Baggioli, M.; Zaccone, A. Anharmonic theory of superconductivity in the high-pressure materials. *Phys. Rev. B* **2021**, *103*, 094519.
(55) Wakita, K.; Shim, Y.; Orudzhev, G.; Mamedov, N.; Hashimzade, F. Band structure and dielectric function of $TlInTe_2$. *Phys. Status Solidi A* **2006**, *203*, 2841−2844.
(56) Orudzhev, G. S.; Godzhaev, É. M.; Kerimova, R. A.; Allakhyarov, É. A. Band structure and optical properties of the $TlInTe_2$ chain compound. *Phys. Solid State* **2006**, *48*, 42−46.
(57) Lifshitz, L. I. Anomalies of Electron Characteristics of a Metal in the High Pressure Region. *J. Exp. Theor. Phys.* **1960**, *11*, 1130−1135.
(58) Kaganov, M. I.; Nurmagambetov, A. A. Generalized topological transition; the surface phase transition of 21/2; *J. Exp. Theor. Phys.* **1982**, *56*, 1331−1333.
(59) Gupta, R.; Xiong, Q.; Adu, C. K.; Kim, U. J.; Eklund, P. C. Laser-induced Fano resonance scattering in silicon nanowires. *Nano Lett.* **2003**, *3*, 627−631.
(60) Cerdeira, F.; Fjeldly, T. A.; Cardona, M. Interaction between electronic and vibronic Raman scattering in heavily doped silicon. *Solid State Commun.* **1973**, *13*, 325−328.
(61) Heyen, E. T.; Cardona, M.; Karpinski, J.; Kaldis, E.; Rusiecki, S. Two superconducting gaps and electron-phonon coupling in $YBa_2Cu_4O_8$. *Phys. Rev. B: Condens. Matter Mater. Phys.* **1991**, *43*, 12958.
(62) Stein, P. V.; Wolf, T.; Renker, B. Electron-phonon coupling in 123-superconductors investigated by Raman scattering. *J. Low Temp. Phys.* **1996**, *105*, 825−830.

https://doi.org/10.1021/acs.inorgchem.0c03795
Inorg. Chem. 2021, 60, 9320−9331